ARTICLE

Check for updates

Stabilized director buckling patterns in nematic elastomers and their dynamic optical effects

Takuya Ohzono [1✉], Hiroyuki Minamikawa[2] & Eugene M. Terentjev[3]

Pearlescence and iridescence, which are a class of light diffusion effects that exhibit sharp viewing-angle-dependent brightness and colors, are important material properties for notification purposes and lighting devices. Here we report elastomeric materials with self-organized periodic birefringent patterns that exhibit these optical effects, with additional dynamic and reversible tunability. A stack of micron-thick layers, each of which has a nematic director tilted from the layer normal in a different direction, assembles a birefringence-pattern-based anisotropic diffuser in a nematic liquid-crystal elastomer. The periodic pattern is formed after buckling induced by the uniaxial thermal shrinkage, and the associated rotation of an initially uniform director state. The patterns can be stabilized by secondary crosslinking. Upon deformation or increasing the temperature, the light diffusion with viewing-angle-dependent colors reversibly fades owing to the diminishing of optical effects via strain-induced alignment or thermal randomization of birefringence, respectively. Such elastomers with tunable self-organized birefringence patterns can be used for reconfigurable optical elements and strain/temperature detection in the form of films, tapes, rods, and fibers.

[1] Research Institute for Electronics and Photonics, National Institute of Advanced Industrial Science and Technology (AIST), 1-1-1 Higashi, Tsukuba 305-8565, Japan. [2] Interdisciplinary Research Center for Catalytic Chemistry, AIST, 1-1-1 Higashi, Tsukuba 305-8565, Japan. [3] Cavendish Laboratory, University of Cambridge, J.J. Thomson Avenue, Cambridge CB3 0HE, UK. ✉email: ohzono-takuya@aist.go.jp

Pearlescence and iridescence are a class of light diffusion or scattering effects that are often observed in nature and exploited as eye-catching aspects for notification purposes and lighting devices, i.e., sign films and sheeting materials. The sharp viewing-angle-dependent brightness and colors of iridescence originate from structural coloration, which is an effect of Bragg scattering displayed by periodic structures featuring different refractive indices and a periodicity near the visible light wavelength[1,2]. In contrast to pigments typically showing degradation of molecular structures[3], the absence of photobleaching in their practical performance is a technological advantage. Several systems containing these periodic structures with various optical functions have been proposed, including surface-micropatterned topographies[4–7], colloids embedded in polymers[8–11], and micropatterns of birefringent materials, such as liquid crystals[12], which were targeted in this study.

In particular, liquid-crystal systems with well-designed alignment patterns composed of low-molecular-weight liquid-crystal molecules in various liquid-crystal phases[13–15] in electrode cells[16–18] facilitate rapid electrical switching of optical effects, such as grating functions. Transiently formed shear band structures[19,20] have been examined in the case of viscous polymers, and optical effects of some of these have been reported[21]. Crosslinked liquid-crystal polymer systems—known as liquid-crystal elastomers (LCEs)—represent the elastic solid version, which retains the mobility of the liquid-crystal director but with the coupling to the elastic deformation field[22]. Typically, LCEs are freestanding materials that often show actuations, which can augment their applications for realizing various optical effects. LCEs in the cholesteric liquid-crystal phase[23–26] with helical photonic structures exhibit selective reflection of circularly polarized light with the same handedness as that of the helical structure and with the wavelength determined by the pitch and the average refractive index. Although cholesteric periodic structures stabilized by polymerization have been comprehensively studied[23–26], other systems have not been sufficiently explored. Even nematic LCEs may have the potential to be employed as optical elements, provided they exhibit specific regular patterns of the optical axis, that is, the nematic director.

Stripe domains, which are probable structures of nematic LCEs suitable for these optical applications, e.g., optical diffusers with pearlescent and iridescent effects, spontaneously self-organize upon uniaxial stretching of a stabilized monodomain state in the direction perpendicular to the alignment[22,27–35]. However, the stripes are generically transient and unstable so that they are easily disarranged by changes in the applied strain. Because the sample edges are typically clamped for stretching, the director rotation upon stripe domain formation is restricted to the film plane, which is characterized by the splitting of the nematic halo peak in wide-angle X-ray scattering (WAXS) data into four directions[27,30]. This results in micrometer-sized stripe domains with alternating director rotation and shear in adjacent domains, which absorb the net strain change with fairly preserving the nematic order upon stretching. The long sides of the stripes are parallel to the stretching direction. This periodic structure may function as a crude optical axis grating. However, the optical properties of stripe domains, including their stability, have not yet been reported, possibly because of their transient (unstable) nature and serious inhomogeneity in the sample, which hinders their application. Characteristics related to the sample shape, such as the aspect ratio, clamping method[27–30], and experimentally uncontrollable stretching angle misfit[31], can also affect the appearance of the inhomogeneity.

To overcome these problems, a new method was developed in this study to homogeneously produce analogous stripe domains over a nematic LCE assisted by thermal uniaxial shrinkage, which yielded materials that are otherwise difficult to realize. It is also discussed that the present stripe domains are critically different from the previously known ones regarding the three-dimensional distribution of directors. Moreover, these were stabilized by secondary crosslinking, which led to dynamic pearlescence that was reversibly tunable by strain and temperature.

Results and discussion

Thermally induced director buckling patterns. The fabricated LCEs comprise three monomers (Fig. 1a) nominally linked via the "click" Michael addition reaction[36–38] between thiols and acrylates in the isotropic phase (Fig. 1b; see Methods for details). The excess of acrylates in the resultant main-chain LCE at room temperature ($T = 22 \,°C$) were left open for photocrosslinking at a later stabilization step. The thiol–ene-linked LCEs were in a polydomain state at room temperature, in which micron-sized nematic domains with different orientations coexisted and strongly scattered light leading to low transparency (Fig. 1c, image of opaque sample)[22,39,40]. The polydomain sample exhibited a nematic–isotropic (NI) transition at $T_{NI} = 78 \,°C$ (Fig. 2a), below which the birefringence required for optical effects was maintained. The polydomain sample was uniaxially stretched at room temperature in the x-direction to a strain of $e = 1.5$ to mechanically align the nematic director, and was subsequently released for free retraction (Fig. 2b). The original shape ($e = 0$) and the polydomain pattern never recovered at room temperature, similar to previously reported behavior of main-chain polydomain LCEs[39], and a residual strain of $e_r \sim 1.05$ emerged as the arrested-state characteristic of the constructed main-chain LCEs.

In previous studies conducted on inducing stripe domains[27–30], aligned and stabilized monodomain samples were clamped and uniaxially stretched in the direction perpendicular to the monodomain director, which simultaneously induced shrinkage in the director direction. The mechanical clamping inevitably induces strain distribution, resulting in inhomogeneous stripe domain formation. However, in the present study, a spontaneous thermal shrinkage process, in which the clamp was unnecessary, was employed to uniformly reduce the natural length in the x-direction over the sample from the elongated state of $e_r \sim 1.05$. Using this method, the induced strain becomes essentially homogeneous over the sample, and thus, inhomogeneous stripe domain formation can be consequently minimized. Annealing at an elevated temperature for only 1 min (annealing step, at a specific temperature of 20, 40, 60, or 80 °C, shown in Fig. 1c) irreversibly induced uniaxial shrinkage in the x-direction (Fig. 3a).

The reduced nematic order achieved by increasing the temperature unlocks a certain degree of entropic elasticity that induces temperature-dependent uniaxial shrinkage of the sample[22]. This corresponds to the generally observed reduction in the soft elastic plateau in their stress–strain curves as the temperature approaches T_{NI}[41]. It is worth noting that the investigated main-chain nematic LCEs were not in an equilibrium state, but in arrested states, probably owing to their relaxation being hindered by the suppressed hairpin dynamics[39,42]. Therefore, each local director could not return toward the original alignment of the initial polydomain pattern upon halfway shrinkage, being unlike non-arrested side-chain LCEs[43] and other reversible cases[39]. Instead, the aligned state ($e = 1.5$) was established as the new reference state, and the directors collectively self-organized to accommodate the net shrinkage and develop the stripe domains. Even before the thermal annealing, spontaneous shrinkage from the highly aligned state ($e = 1.5$) to the arrested one ($e_r \sim 1.05$) induced a dim stripe domain, as shown later. The different tilting
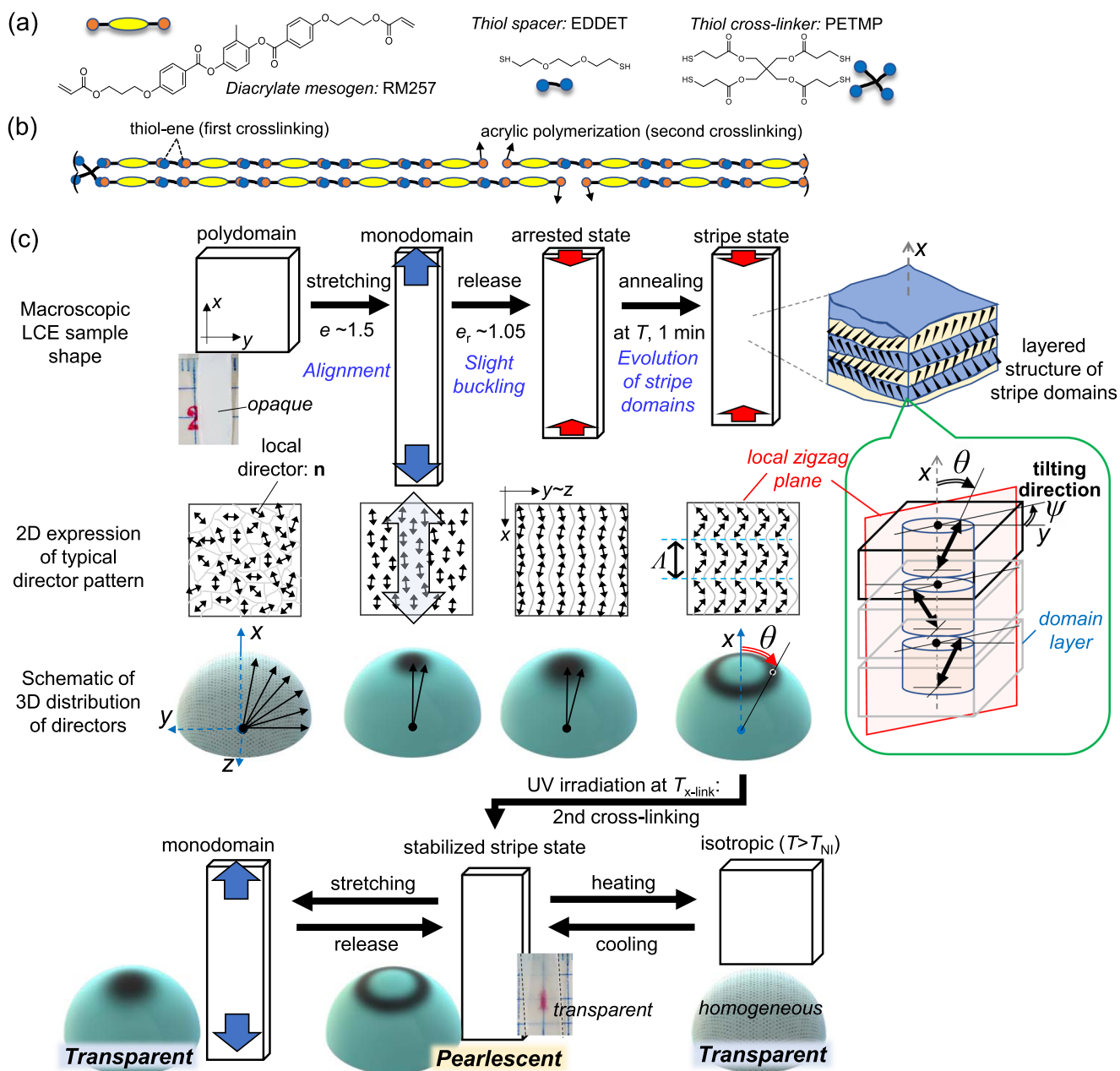
Fig. 1 Preparation of LCEs with stabilized director patterns. a Chemical formulae of the main-chain LCE components. **b** Schematic of a nominal polymeric unit. **c** Detailed illustrations of the preparation and director states of the LCEs showing the macroscopic sample shapes, typical director patterns, and their distributions on a hemisphere.

directions of the neighboring domain layers and the collective tilting can minimize the average network strain and Frank elastic energy, respectively, similar to previously reported stripe domain formations[27–30]. This process possibly follows a formation mechanism similar to that of the shear band structures in viscous polymers[19].

The periodicity of the examined stripe domains ($\Lambda \sim 1.3\,\mu m$) was characterized by monochromic light-scattering (LS, 633 nm) patterns (Fig. 3b) and polarized fluorescence optical microscopy (PFOM; Fig. 3c). Initially, a dim stripe pattern was visible only in the contrast-enhanced PFOM image acquired at 22 °C. The PFOM contrast increased with increasing temperature, and the first-order LS diffraction peaks became evident, suggesting the growth of distinct stripes. The PFOM image obtained at 50 °C shows disordered stripes containing oblique thin darker lines in the bright stripes. The stripe pattern vanished at 80 °C (> T_{NI}; isotropic phase), as characterized by the disappearance of the LS diffraction peaks (Fig. 3c).

Stabilization of director buckling patterns. It is worth noting that the annealing-induced stripe patterns slightly coarsened with time and were readily and irreversibly distorted upon mechanical perturbation (Supplementary Fig. 1). This fragility is inappropriate to the steady use of the stripe patterns. The structures should be in an arrested state and exhibit extremely slow relaxation[39], which transiently keeps the stripe domain. Therefore, secondary crosslinks were introduced between the residual acrylates immediately after the thermal shrinkage at a specific temperature (T_{x-link}) (Fig. 1c) to stabilize the transient stripe patterns against thermal and mechanical perturbation. Figure 4a shows the PFOM, LS, and WAXS patterns of the stabilized
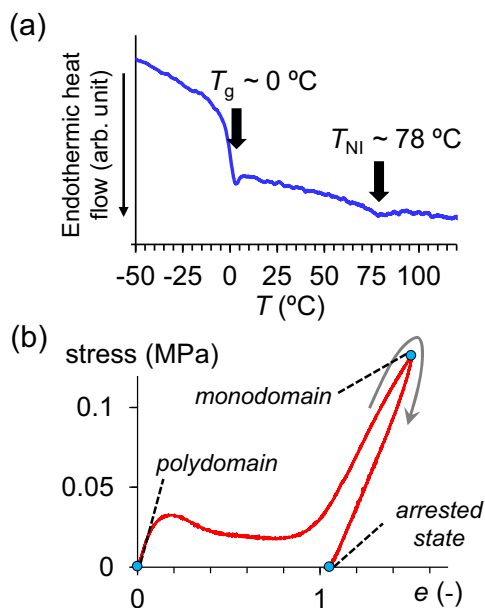
(a)

(b)

Fig. 2 Thermal and mechanical properties of LCE after the first crosslinking. a DSC heating curve of the LCE acquired at 5 °C/min prior to the second crosslinking. **b** Stress–strain (SS) curve of the LCE in a strain cycle of $0 \rightarrow 1.5 \rightarrow 0$ in the x-direction measured at a strain rate of $0.0033\,s^{-1}$ prior to the second crosslinking. A residual strain of $e_r \sim 1.05$ emerged as the arrested state after strain release.

samples at room temperature. The similarity of these PFOM and LS patterns to the pre-stabilization patterns (Fig. 3b, c) confirm that the transient structures were safely fixed without considerable structural changes.

In particular, the samples stabilized at $T_{x\text{-link}} = 40$ °C and 60 °C maintained clear stripes and anisotropic LS, suggesting their usefulness as optical elements with anisotropic light diffusion with the wavelength dispersion. The anisotropic WAXS patterns obtained in all cases indicate director alignment in the x-direction on average. However, the macroscopic anisotropy diminished with increasing $T_{x\text{-link}}$, suggesting that the director tilting proceeded because of the higher shrinkage at a higher $T_{x\text{-link}}$ (Fig. 3a). This result is also supported by the dichroic intensity differences in the PFOM images acquired using different polarizer angles (Supplementary Fig. 2). Even for the sample stabilized at $T_{x\text{-link}} = 80$ °C, the leftover blurred stripes are consistent with the slightly anisotropic WAXS pattern (Fig. 4a), suggesting that the original isotropic state was not fully recovered by the one-minute annealing. However, the corresponding LS pattern is almost isotropic owing to the disordered periodic structures at the visible light wavelength scale.

Three-dimensional structure of director buckling patterns. The WAXS patterns of the nematic halo also suggest a critical difference between the present system and the previously reported stripe domains formed by clamp-assisted mechanical stretching[22,27,30], with the latter believed to consist of two domains with both directors confined to the film plane, which corresponds to the xy-plane in this study. This scenario was characterized by the splitting of the WAXS peak into four points in the full WAXS pattern, which corresponds to the splitting of the single WAXS peak in Fig. 4a into two parts (top and bottom). However, the investigated system did not display this split, suggesting that the directors were not confined to the xy-plane on average, and the tilting direction (ψ) in Fig. 1c was possibly selected at random. This is also evidenced by the observation of a

similar stripe pattern on the xz-cross-section (Supplementary Fig. 3).

The non-split WAXS peak could also be interpreted as a smooth variation of the directors over the stripe boundaries[20], that is, sinusoidal or serpentine structures rather than zigzags. However, this can presumably be ruled out by the flat plateaus and bases of the domains in the fluorescence intensity profiles (I_{flu} profile in Fig. 4b), which reveal zigzags with relatively sharp domain boundaries.

As the observed buckling or meandering of the monodomain director state was induced by thermal uniaxial shrinkage without any external constraints on strain and stress (that is, no clamps), any director tilting direction (ψ) from the x-axis can be selected for a certain domain layer, being based on the simple symmetry argument. This symmetry is likely similar to the classical Euler buckling of a cylindrical slender rod under compressive strain along the long axis, where the deflection direction from the compression axis is arbitrary[44]. The three-dimensional distribution of directors, their spatial correlations, and the layered structure subsequently became curious for analysis (schematics in Fig. 1c). However, analyzing these aspects by PFOM was difficult because it only probed the surface; moreover, a depth of only tens of micrometers could be imaged even with the confocal version.

Nevertheless, the representative tilting angle, θ, of the directors from the x-axis was analyzed using the PFOM images (Fig. 4b, c), in which the nematic director components projected onto the xy-plane were reflected. In contrast to POM (Supplementary Fig. 4), the nematic orientation was directly determined by PFOM as the maximum of the polarized fluorescence intensity achieved by altering the polarizer angle (φ). Certain points in the data (circles in Fig. 4b, c) with a higher contrast in the images were analyzed, avoiding the sharp domain boundary regions. A smaller value of θ $\sim \pm 30°$ was expectedly achieved at $T_{x\text{-link}} = 40$ °C compared to the $\pm 40°$ obtained at $T_{x\text{-link}} = 60$ °C, because of the smaller shrinkage of the former during thermal annealing (Fig. 3a).

Light-scattering property. The angle-dependent scattering intensities of the transmitted white light in the x- and y-directions at three different wavelengths and the experimental setup are shown in Fig. 4d–f. The samples with tangible stripe patterns in the PFOM images, obtained at $T_{x\text{-link}} = 40$ and 60 °C, exhibited angle-dependent scattering with a wavelength dependence (iridescence), similar to a crude grating. Although the observed diffraction efficiency was low (a few %; Fig. 4d, e, g), the optical effects (pearlescence and iridescence) were clearly visible to the naked eye (Supplementary Movie 1).

A cylindrical sample with a diameter of ~5 mm, in which the rotational symmetry exists with respect to the x-axis, and thus, there is no distinction between the y and z direction, exhibited a similar anisotropic scattering independent of the sample rotation around the x-axis (Supplementary Fig. 5), further confirming the uniform distribution of the tilting direction on average. If the diameter is reduced, the pearlescent fiber may be fabricated. Moreover, the scattering property was insensitive to the aspect ratio of the film, and the scattering was homogeneous over the sample (Supplementary Fig. 6). These results indicate critical differences of these domains from the previously reported inhomogeneous stripe domain formations with directors confined to the xy-plane[27–31]. The direct transmittance monotonically decreased with increasing $T_{x\text{-link}}$ (Fig. 4g), suggesting the disordering of periodic structures owing to the larger shrinkage and the lower nematic order upon stabilization.

Assuming a simple amplitude grating, the periodicity (d) responsible for the first-order scattering angle of $\Omega \sim 32°$ in the x-direction of the ~700-nm light observed on the sample prepared
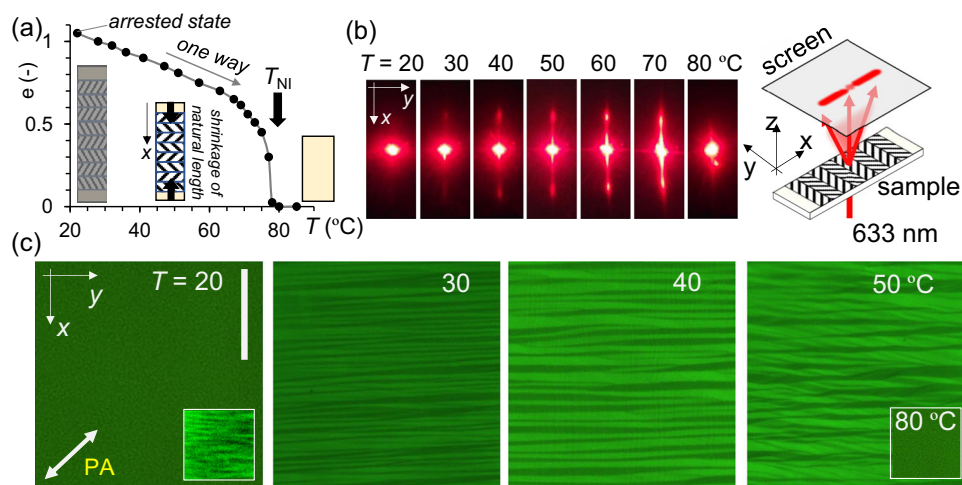
Fig. 3 Effects of thermal annealing on the arrested LCE. a Natural length shrinkage of the arrested LCE with increasing annealing temperature. The sample uniaxially contracts irreversibly and the original shape is recovered upon crossing T_{NI}. **b** Evolution of light-scattering (LS) patterns (633 nm) of non-polarized light without an analyzer. The first diffraction peaks increase in intensity with temperature and disappear at T_{NI}. **c** Polarized fluorescence optical microscopy (PFOM) images obtained under identical conditions at different temperatures, showing stripe patterns with their wave vector in the x-direction. The insets in the image acquired at 20 and 80 °C show a contrast-enhanced version with visible blurred stripes and absence of stripes, respectively.

with $T_{\text{x-link}} = 40\,°C$ can be estimated as follows: $d = \lambda/\sin\Omega$ $\sim 1.32\,\mu m$. This value is consistent with that estimated via PFOM ($\Lambda \sim 1.3\,\mu m$). As the sample surface is almost flat (Supplementary Fig. 7), which is different from topographic diffusers[6,45], the investigated system is presumably a grating with phase retardation occurring inside the sample[13–15]. As each nematic LCE typically exhibits a unique temperature-dependent birefringence, the periodic variations of the optical axis with $\Lambda \sim 1.3\,\mu m$, as observed in the stripe patterns, likely construct the optical axis grating, by which the polarization of diffracted light is often modulated, at least locally in the sample. Unfortunately, the investigated self-organized three-dimensional layered structure contained several unknown irregularities, for example, in the periodicity, tilting directions, and layer thickness, compared to microfabricated optical axis gratings, such as liquid-crystal-based Pancharatnam–Berry phase devices[16,46].

Although clear phase modulation was not expected, the polarization states were briefly characterized using a polarizer and analyzer (Supplementary Fig. 8a). The results show that the first-order diffraction band was polarized in the x-direction and originated from the y-polarized incident light component (Yx mode in Supplementary Fig. 8a). This depolarization may result from the addition of two counter-rotated, elliptically polarized, diffracted light beams with a phase difference of π (Supplementary Fig. 8b). The diffracted light from domains with positive θ clearly had an identical scattering interference angle (Ω) to that of the alternative domains with negative θ, because the periodicity (Λ) was common, at least locally, for the neighboring domains. Notably, the phases of the first-order interference light differed by π because of their positional difference (Λ/2) in the x-direction (Supplementary Fig. 8b). Moreover, the rotations of the elliptical polarization, which resulted from the birefringent domains with optical axes having inversion symmetry with the yz-plane, were opposite to each other. Consequently, the polarization of the first-order diffractions might be rotated by 90°.

An imperfect periodic structure and the distribution of tilting directions may induce blurring of the propagating light owing to the spatial optical-phase non-uniformity, resulting in random walk-off[47] and depolarization. This blurring was indeed observed on the thicker sample (Supplementary Fig. 9). Nevertheless, the observed anisotropic scattering of the transmitted light, that is, pearlescence and iridescence, remained sufficiently strong for naked-eye detection even at a thickness of ~1 mm. In contrast to the highly opaque polydomain samples, the zeroth-order transmittance of the synthesized LCEs was relatively high; the directly reflected anisotropic scattering is weak. Therefore, an LCE film supported by a mirror also exhibited similar optical effects in the reflection mode (Supplementary Fig. 10), widening its application range.

Dynamic optical effects. The aforementioned optical effects of the stabilized layered structures with buckled nematic directors were dynamically tuned further by external perturbations (strain or temperature; Fig. 5). Although the soft elasticity was suppressed by the secondary crosslinking and led to elastic behavior (Fig. 5a), stretching in the x-direction gradually rotated the directors to reversibly align them in the mono-domain state with a slight viscoelastic delay in their mechanical response. This was accompanied by continuous fading of the layered structure, resulting in a transparent nematic mono-domain state with diminished pearlescence and iridescence (Fig. 5b and Supplementary Movies 2, 3). The ability to dynamically tune the optical effect can be utilized as elements of smart systems, for example, the lighting and sign films, in which the eye-catching pearlescent/diffusion and the less-visible transparent states can be switched on demand. Moreover, dynamic tunability was realized in water (Supplementary Movie 4) and was stable against mechanical rubbing (Supplementary Movie 5), demonstrating a certain level of robustness of the material for outdoor uses, e.g., luminaries, smart windows, and sign sheeting.

The scattering also diminished with increasing temperature because the birefringence monotonically decreased with decreasing nematic order (Fig. 5c). Although the temperature-dependent optical effect is reversible and repeatable, it accompanies actuation, which could change the sample area, depending on the temperature, similar to previously reported LCE systems[22,48,49], which can be minimized by increasing the density of the secondary crosslinks or coercively fixing the strain as required.
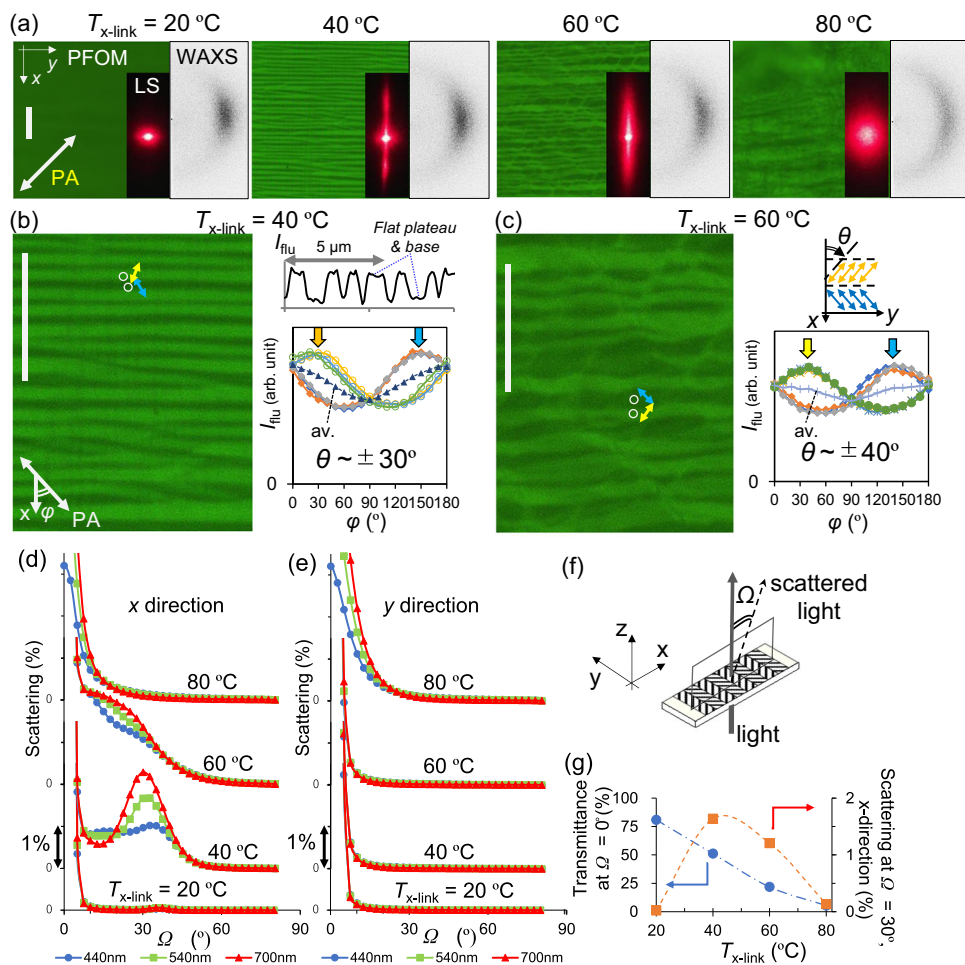
Fig. 4 LCEs with stabilized buckled director patterns. a Room-temperature PFOM, LS, and WAXS patterns of LCEs prepared using different crosslink temperatures ($T_{\text{x-link}}$). Analysis of directors at LCE surfaces fabricated at **b** $T_{\text{x-link}} = 40$ °C and **c** 60 °C. The typical intensity profile (in **b**), magnified PFOM images, and the polarized fluorescence intensity (I_{flu}) at specific locations as a function of polarizer angle (φ) are shown (scale bar: 10 μm). The white circles indicate the typical measurement positions for the φ–I_{flu} plots (details provided in the main text). The tilting angle (θ) can be estimated from the peaks of the φ–I_{flu} plots. Angle-dependent scattering intensities of LCEs in the **d** x- and **e** y-directions at different wavelengths (440, 540, and 700 nm). Each curve is vertically shifted for visibility (note each zero point). The sample crosslinked at 40 °C, in particular, exhibited pearlescence with iridescence. **f** Experimental setup for the scattering intensity measurements. **g** Transmittance at $\Omega = 0$° and 30° in the x-direction plotted against $T_{\text{x-link}}$.

Conclusion

In conclusion, the fabrication and stabilization of a new class of periodic layered birefringent structures self-organized within a nematic LCE were discussed herein. The present stripe domains are critically different from the previously known ones[22,27–35] regarding the three-dimensional distribution of directors; the tilting directions of directors from the pre-stretched axis are not limited to a specific plane in the present LCE. The stripe domains formed as periodically buckled director patterns, emerging upon uniaxial thermal shrinkage in main-chain LCEs with the arrested relaxation[39], were stabilized by the additional crosslinking. These periodic structures exhibited anisotropic light-scattering effects (pearlescence and iridescence), and were susceptible to dynamic and reversible tuning with changes in the applied strain or temperature. Using such a system in reverse presents the option of a sensor, optically detecting strain or temperature changes from the change in scattering patterns. The developed system presented attractive features such as the dynamic tunability of optical effects in the visible light range, straightforward fabrication within thick films without surface alignment due to self-organization, simplicity of the single-component material, and mechanical robustness. Therefore, the constructed LCEs with a unique layered structure can be employed in a broad class of switchable optical elements for realizing augmented luminaries, smart windows, and sign sheeting applications.

Methods

Materials and preparation of LCEs. Previously reported methods[36–38] were followed for preparing the LCEs, which involved two-step crosslinking reactions, a Michael addition reaction between acrylates and thiols, and a photoinduced radical polymerization of diacrylates, with slight modifications. The diacrylate monomer, 2-methyl-1,4-phenylene bis(4-(3-(acryloyloxy)propoxy)benzoate) (RM257), was purchased from Wilshire Technologies (Fig. 1a). Two thiol monomers, 2,2'-(ethylenedioxy) diethanethiol (EDDET) and pentaerythritol tetrakis (3-mercaptopropionate) (PETMP), were purchased from Sigma Aldrich. Triethylamine (TEA, Sigma Aldrich) was used as the Michael addition catalyst. Irgacure2959 (BASF) was used as a photoinitiator, and butylated hydroxytoluene (BHT, Sigma Aldrich) was used as a radical scavenger to suppress the undesirable radical polymerization of acrylates. Toluene (Sigma Aldrich) was used as the solvent for the first crosslinking reaction. Coumarin 545 T (C5T, Tokyo Chemical Industry)[50,51] was used as a dichroic fluorescent probe, and dimethylformamide (DMF, Sigma Aldrich) was used as a solvent for the dye solutions. All chemicals were used in the as-received conditions without purification. RM257, EDDET, and PETMP were weighed at specific molar ratios of 54:43:3. Toluene (30 wt.%), Irgacure2959 (0.2 wt.%), and BHT (0.5 wt.%) were added. After the mixture was gently mixed at an elevated temperature (~80 °C) for ~10 min, TEA (1.5 wt.%) was added to initiate the Michael addition reaction between the thiol and acrylate groups. The mixture was molded between two glass slides with 0.4-mm-thick spacers at 80 °C (isotropic phase) overnight. A glass tube with an inner diameter of ~4 mm was used as a mold to prepare the cylindrical rod sample. Notably, no surface alignment was required. The sample was subsequently peeled and annealed at 80 °C in
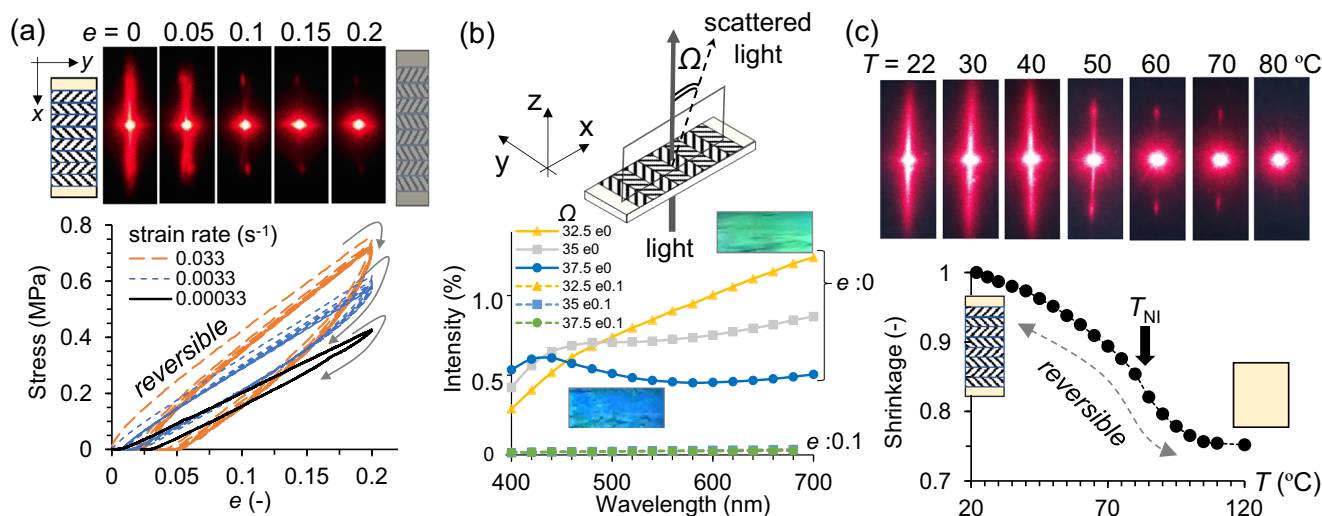
Fig. 5 Dynamic optical effects of LCEs with stabilized buckled director patterns. a LS patterns obtained at different applied uniaxial strains (top) and stress–strain curves acquired at different strain rates (bottom). The LS patterns are of the slowest strain rate. **b** Angle-dependent spectra of scattered light obtained with ($e = 0.1$) and without strain ($e = 0$). The insets show sample images with a sharp angle-dependency of colors (iridescence) at $e = 0$. **c** LS patterns obtained at different temperatures (top) and the corresponding temperature-dependent strain (bottom).

a vacuum oven for 12 h to evaporate the solvent. The sample was cooled thereafter to room temperature to obtain pre-crosslinked samples exhibiting polydomain patterns. Samples were cut and subsequently used to generate stripe domains. The pre-crosslinked samples were uniaxially stretched up to a strain of ~1.5 (2.5 times in length) at a strain rate of ~0.1 s^{-1} and at room temperature (nematic). Each sample, which was subsequently released from the clamps, exhibited spontaneous shrinkage to a residual strain of ~1.05. The sample was subsequently placed on a hotplate or in an oven at $T = T_{x\text{-link}}$ (20–80 °C) for 1 min to enable thermal uniaxial shrinkage for stripe domain formation and irradiated with UV light (365 nm) for 20 min to stabilize the stripe domain by completing the crosslinking reaction between the remaining acrylates.

Differential scanning calorimetry (DSC). Pre-crosslinked samples (~15 mg) were loaded into standard aluminum DSC pans for DSC analysis (DSC6100 SII Nanotechnology). The samples were cooled to −60 °C at −5 °C min^{-1} and heated to 110 °C at 5 °C min^{-1} to acquire the initial heating data. The glass transition temperature was identified as the temperature with a baseline shift in the low-temperature range. The samples were scanned in three heating runs ($N = 3$).

Wide-angle X-ray scattering (WAXS). The phases of the LCEs at room temperature were characterized using a Rigaku type 4037 diffractometer with graded d-space elliptical side-by-side multilayer optics, monochromated Cu Kα radiation (wavelength, 0.1542 nm; 40 kV; 30 mA), a flat camera with an imaging plate (R-Axis IV, Rigaku), and a temperature control unit (FP82HT, Mettler). An exposure time of 5 min and a sample-to-camera length of 150 mm were used.

Stress–strain response. The stress–strain curves of the LCE films in the tensile mode at room temperature were obtained using a commercial instrument (EMX1000, IMADA) at room temperature. The typical sample width and effective length were 5 and 30 mm, respectively.

Polarized fluorescence optical microscopy (PFOM). The samples were dyed to facilitate PFOM analysis. To dye a sample, a 5 µL droplet of 0.2 wt.% C5T in DMF was cast on the sample surface at 80 °C, and the sample was subsequently placed in a vacuum oven at 80 °C for ~6 h to ensure solvent evaporation prior to characterization. To characterize the sample cross-sections, a sample frozen at −18 °C was cut to yield xz- and yz-planes, which were subsequently dyed using the aforementioned protocol. A conventional fluorescence optical microscope with polarizers was employed, in which the light source was mounted above the sample and the excitation light was passed through a microscope objective lens prior to reaching the sample. A Xe lamp (75 W) was used as the light source. A fluorescence filter set (U-MWIB-3, Olympus), which comprised an excitation filter that transmitted light at wavelengths between 460 nm and 495 nm, and an emission filter that transmitted light with wavelengths longer than 510 nm, was used to detect the emission from fluorescence probes. The images were collected at a pixel size of 0.154 µm using a Nikon DS-Ri2 camera connected to a computer and controlled using imaging software (NIS-Elements, Nikon). An objective lens with a numerical aperture of 0.75 (MPLFLN-BDP50x, Olympus) was used. Linearly polarized

excitation was employed, and the polarized fluorescence intensities were measured under identical polarization conditions. The focus was carefully adjusted to the top surface, where the contrast was the highest. The dichroic contrast was enhanced using a positive dichroic dye[51]. The brighter parts of the PFOM images indicate that the absorption and fluorescence transition dipole moment vectors of the probe have more components in the polarizer direction. As the employed dye molecules aligned in parallel with the nematic directors of the LCEs, the domains resolved by PFOM directly reflected the stripe domain in two dimensions. As the polarizers were placed along the x-axis, the fluorescence intensity reflected the x-component, n_x, of the director, **n**. When the polarizers (or the sample) were rotated, the brightest or darkest parts gradually became darker or brighter, respectively. The temperature (T) of the sample was controlled on a transparent hot stage (Tokai-Hit, Co., Ltd.) with multiple thermocouples around the observation point. T was changed at a rate less than ~0.01 °C s^{-1}.

Light scattering (LS). A He–Ne laser (wavelength, 632.8 nm; 1 mW; Melles Griot 05-LHP-111) was used for the LS experiments[52]. The incident light was depolarized using a quartz depolarizer (SigmaKoki). The sample was placed between a set of polarizers under crossed/parallel-Nicol conditions in the depolarized LS experiments. The laser light diameter was ~0.6 mm, and the scattering pattern was captured on a paper screen placed 20-mm away from the sample using a digital camera. The same position on the sample was observed by microscopy using the temperature-controlled setup.

Angle-dependent spectra of scattered light. The spectra of the scattered light at different scattering angles were acquired using a spectrophotometer (GC 5000, Nippon Denshoku Industries) to characterize pearlescence. The diameter of the incident white light was ~5 mm, and the transmitted/reflected scattered light was collected at different angles with a wavelength resolution of 20 nm. For the transmission and reflection modes, 100 % light intensity was normalized by the sample-free intensity obtained at 0°, and the intensity at 0° obtained using a standard white plate (Nippon Denshoku Industries), respectively.

Atomic force microscopy. The surface topology was imaged using an atomic force microscope (AFM, 5400, Agilent) in tapping mode with a sharp tip (SI-DF20S; tip radius, 2–5 nm; spring constant, $k \sim 12$ N m^{-1}; SII).

Data availability

7

References

1. England, G. T. & Aizenberg, J. Emerging optical properties from the combination of simple optical effects. *Rep. Prog. Phys.* **81**, 016402 (2018).
2. Kinoshita, S., Yoshioka, S. & Miyazaki, J. Physics of structural colors. *Rep. Prog. Phys.* **71**, 076401 (2008).
3. Pfaff, G. & Reynders, P. Angle-dependent optical effects deriving from submicron structures of films and pigments. *Chem. Rev.* **99**, 1963–1981 (1999).
4. Hsiung, B.-K. et al. Tarantula-inspired noniridescent photonics with long-range order. *Adv. Opt. Mater.* **5**, 1600599 (2017).
5. Umh, H. N., Yu, S., Kim, Y. H., Lee, S. Y. & Yi, J. Tuning the structural color of a 2D photonic crystal using a bowl-like nanostructure. *ACS Appl. Mater. Interfaces* **8**, 15802–15808 (2016).
6. Ohzono, T., Suzuki, K., Yamaguchi, T. & Fukuda, N. Tunable optical diffuser based on deformable wrinkles. *Adv. Opt. Mater.* **1**, 374–380 (2013).
7. Yamashita, K., Kunitsu, K., Hattori, T., Kuwahara, Y. & Saito, A. Demonstration of a diffraction-based optical diffuser inspired by the Morpho butterfly. *Opt. Express* **29**, 30927 (2021).
8. Holtz, J. H. & Asher, S. A. Polymerized colloidal crystal hydrogel films as intelligent chemical sensing materials. *Nature* **389**, 829–832 (1997).
9. Li, M. et al. Supramolecular photonic elastomers with brilliant structural colors and broad-spectrum responsiveness. *Adv. Funct. Mater.* **30**, 2000008 (2020).
10. Ohtsuka, Y. et al. Stimuli-responsive structural colored gel that exhibits the three primary colors of light by using multiple photonic band gaps acquired from photonic balls. *ACS Appl. Mater. Interfaces* **12**, 54127–54137 (2020).
11. Ye, Y. N. et al. Flower-like photonic hydrogel with superstructure induced via modulated shear field. *ACS Macro Lett.* **10**, 708–713 (2021).
12. Zola, R. S. et al. Dynamic control of light direction enabled by stimuli-responsive liquid crystal gratings. *Adv. Mater.* **31**, 1806172 (2019).
13. Serak, S., Tabiryan, N. & Zeldovich, B. High-efficiency 15 μm thick optical axis grating and its use for laser beam combining. *Opt. Lett.* **32**, 169 (2007).
14. Jiang, M. et al. Liquid crystal Pancharatnam–Berry micro-optical elements for laser beam shaping. *Adv. Opt. Mater.* **6**, 1800961 (2018).
15. Marrucci, L., Manzo, C. & Paparo, D. Pancharatnam-Berry phase optical elements for wave front shaping in the visible domain: Switchable helical mode generation. *Appl. Phys. Lett.* **88**, 221102 (2006).
16. Sarkissian, H. et al. Polarization-controlled switching between diffraction orders in transverse-periodically aligned nematic liquid crystals. *Opt. Lett.* **31**, 2248 (2006).
17. Crawford, G. P., Eakin, J. N., Radcliffe, M. D., Callan-Jones, A. & Pelcovits, R. A. Liquid-crystal diffraction gratings using polarization holography alignment techniques. *J. Appl. Phys.* **98**, 123102 (2005).
18. Provenzano, C., Pagliusi, P. & Cipparrone, G. Highly efficient liquid crystal based diffraction grating induced by polarization holograms at the aligning surfaces. *Appl. Phys. Lett.* **89**, 121105 (2006).
19. Viney, C. & Putnam, W. S. The banded microstructure of sheared liquid-crystalline polymers. *Polymer* **36**, 1731–1741 (1995).
20. Godinho, M. H. et al. Liquid crystalline cellulose derivative elastomer films under uniaxial strain. *Cellulose* **16**, 199–205 (2009).
21. Viney, C. & Windle, A. H. On predicting the optical diffraction pattern from thermotropic specimens having a banded texture. *Polymer* **27**, 1325–1331 (1986).
22. Warner, M. & Terentjev, E. M. *Liquid Crystal Elastomers*. (Oxford Univ. Press, 2007).
23. Bermel, P. A. & Warner, M. Photonic band structure of cholesteric elastomers. *Phys. Rev. E* **65**, 056614 (2002).
24. Warner, M., Terentjev, E. M., Meyer, R. B. & Mao, Y. Untwisting of a cholesteric elastomer by a mechanical field. *Phys. Rev. Lett.* **85**, 2320–2323 (2000).
25. Cicuta, P., Tajbakhsh, A. R. & Terentjev, E. M. Photonic gaps in cholesteric elastomers under deformation. *Phys. Rev. E* **70**, 011703 (2004).
26. Zhang, P., Zhou, G., Haan, L. T. & Schenning, A. P. H. J. 4D chiral photonic actuators with switchable hyper-reflectivity. *Adv. Funct. Mater.* **31**, 2007887 (2021).
27. Kundler, I. & Finkelmann, H. Strain-induced director reorientation in nematic liquid single crystal elastomers. *Macromol. Rapid Commun.* **16**, 679–686 (1995).
28. Finkelmann, H., Kundler, I., Terentjev, E. M. & Warner, M. Critical stripe-domain instability of nematic elastomers. *J. Phys. II* **7**, 1059–1069 (1997).
29. Verwey, G. C., Warner, M. & Terentjev, E. M. Elastic instability and stripe domains in liquid crystalline elastomers. *J. Phys. II* **6**, 1273–1290 (1996).
30. Zubarev, E. R., Kuptsov, S. A., Yuranova, T. I., Talroze, R. V. & Finkelmann, H. Monodomain liquid crystalline networks: reorientation mechanism from uniform to stripe domains. *Liq. Cryst.* **26**, 1531–1540 (1999).
31. Zhang, Y., Zhang, Z. & Huo, Y. Nucleation and critical conditions for stripe domains in monodomain nematic elastomer sheets under uniaxial loading. *J. Mech. Phys. Solids* **144**, 104110 (2020).
32. Mihai, L. A. & Goriely, A. Instabilities in liquid crystal elastomers. *MRS Bull.* **46**, 784–794 (2021).
33. Mistry, D. & Gleeson, H. F. Mechanical deformations of a liquid crystal elastomer at director angles between 0° and 90°: Deducing an empirical model encompassing anisotropic nonlinearity. *J. Polym. Sci. Part B Polym. Phys.* **57**, 1367–1377 (2019).
34. Fried, E. & Sellers, S. Soft elasticity is not necessary for striping in nematic elastomers. *J. Appl. Phys.* **100**, 043521 (2006).
35. De Luca, M., Desimone, A., Petelin, A. & Čopič, M. Sub-stripe pattern formation in liquid crystal elastomers: experimental observations and numerical simulations. *J. Mech. Phys. Solids* **61**, 2161–2177 (2013).
36. Nair, D. P. et al. Two-stage reactive polymer network forming systems. *Adv. Funct. Mater.* **22**, 1502–1510 (2012).
37. Yakacki, C. M. et al. Tailorable and programmable liquid-crystalline elastomers using a two-stage thiol-acrylate reaction. *RSC Adv.* **5**, 18997–19001 (2015).
38. Saed, M. O. et al. High strain actuation liquid crystal elastomers via modulation of mesophase structure. *Soft Matter* **13**, 7537–7547 (2017).
39. Ohzono, T., Katoh, K., Minamikawa, H., Saed, M. O. & Terentjev, E. M. Internal constraints and arrested relaxation in main-chain nematic elastomers. *Nat. Commun.* **12**, 787 (2021).
40. Ohzono, T., Katoh, K. & Terentjev, E. M. Microscopy of diffuse nematic–isotropic transition in main-chain nematic liquid-crystal elastomers. *Macromolecules* **54**, 3678–3688 (2021).
41. Ohzono, T., Minamikawa, H., Koyama, E. & Norikane, Y. Unlocking entropic elasticity of nematic elastomers through light and dynamic adhesion. *Adv. Mater. Interfaces* **8**, 2100672 (2021).
42. Adams, J. M. & Warner, M. Hairpin rubber elasticity. *Eur. Phys. J. E* **16**, 97–107 (2005).
43. Urayama, K., Honda, S. & Takigawa, T. Slow dynamics of shape recovery of disordered nematic elastomers. *Phys. Rev. E* **74**, 041709 (2006).
44. Timoshenko, S. & Gere, J. M. *Theory of Elastic Stability*. (McGraw-Hill, 1961).
45. Harrison, C., Stafford, C. M., Zhang, W. & Karim, A. Sinusoidal phase grating created by a tunably buckled surface. *Appl. Phys. Lett.* **85**, 4016–4018 (2004).
46. Yu, N. & Capasso, F. Flat optics with designer metasurfaces. *Nat. Mater.* **13**, 139–150 (2014).
47. Sarkissian, H., Park, B., Tabirian, N. & Zeldovich, B. Periodically aligned liquid crystal: potential application for projection displays. *Mol. Cryst. Liq. Cryst.* **451**, 1–19 (2006).
48. Küpfer, J. & Finkelmann, H. Nematic liquid single crystal elastomers. *Macromol. Rapid Commun.* **12**, 717–726 (1991).
49. Ohm, C., Brehmer, M. & Zentel, R. Liquid crystalline elastomers as actuators and sensors. *Adv. Mater.* **22**, 3366–3387 (2010).
50. Chen, C. H. & Tang, C. W. Efficient green organic light-emitting diodes with sterically hindered coumarin dopants. *Appl. Phys. Lett.* **79**, 3711–3713 (2001).
51. Ohzono, T., Yatabe, T., Wang, C., Fukazawa, A. & Yamaguchi, S. Negative fluorescence anisotropy of phosphole oxide-based dyes in nematic liquid crystals. *Commun. Chem.* **1**, 52 (2018).
52. Clarke, S. M., Terentjev, E. M., Kundler, I. & Finkelmann, H. Texture evolution during the polydomain-monodomain transition in nematic elastomers. *Macromolecules* **31**, 4862–4872 (1998).

Acknowledgements

Author contributions

T.O. performed experiments. WAXS was performed by H.M. T.O., H.M., and E.M.T analyzed experimental data and contributed to writing and discussing the manuscript.

Competing interests

The authors declare no competing interests.

Additional information

Supplementary information The online version contains supplementary material available at https://doi.org/10.1038/s43246-022-00253-3.

Correspondence and requests for materials should be addressed to Takuya Ohzono.

Peer review information *Communications Materials* thanks the anonymous reviewers for their contribution to the peer review of this work. Primary handling editor: John Plummer.

Reprints and permission information is available at http://www.nature.com/reprints

Publisher's note Springer Nature remains neutral with regard to jurisdictional claims in published maps and institutional affiliations.